Laboratory Measurements on Electric and Elastic Properties of Fractured Geothermal Reservoir Rocks Under Simulated EGS Conditions

Kazuki Sawayama[1], Keigo Kitamura[2] and Yasuhiro Fujimitsu[3]

[1] Department of Earth Resources Engineering, Graduate school of Engineering, Kyushu University, Fukuoka, Japan
[2] International Institute for Carbon-Neutral Energy Research, Kyushu University, Fukuoka, Japan
[3] Department of Earth Resources Engineering, Faculty of Engineering, Kyushu University, Fukuoka, Japan

ABSTRACT

For developing the technique of Enhanced Geothermal System (EGS), the estimation of injected water distribution is essential. To estimate water saturation changes deep under the ground, geophysical explorations (e.g., seismic and electromagnetic explorations) have been applied; however, the relationship between the electric/elastic properties and the water saturation in reservoir rocks has not been well known. Our goal is to elucidate this basic relationship as well as effects of salinity and fracture porosity on it via fluid-flow experiments for more quantitative interpretation of geophysical explorations. In this research, we prepared two types of specimen from geothermal reservoir rocks; A) contains artificially induced thermal cracks (porosity = 10.5%) and B) initially contains a single fracture (porosity = 3.8%). In fluid-flow tests, specimens were initially filled with nitrogen gas (10 MPa of pore pressure) under 20 MPa of confining pressure; the gas emulates the superheated steam that is observed in the geothermal fields. Then, brine (0.1 and 1wt%-KCl) which emulates the artificial recharge to the reservoir, was injected into the samples (11-16 MPa of injection pressure). During the tests, water saturation, permeability, complex resistivity (in the frequency range of 10-2-105 Hz) and elastic wave velocity were simultaneously measured. As a result of Type A specimen, resistivity dramatically decreased from 104 to 102 Ω due to the brine injection. However, P-wave velocity was almost constant (the difference was less than 1%) at that time. These results indicate that resistivity could be sensitive to minor changes in water saturation in the reservoirs compared with P-wave velocity. As a result of Type B specimen, we observed salinity effect on resistivity

(the resistivity difference between 0.1 and 1wt%-KCl brine was almost twice) and its decreasing trend against the water saturation was different from the result of Type A specimen. These dependencies (water saturation, salinity, and porosity) on resistivity could be explained by the total ion content within a specimen.

1. Introduction

Estimating the underground water distribution is essential to develop the geothermal resources not only for monitoring the reservoir condition (recovering or depleting), but also for developing Enhanced Geothermal System (EGS). In previous EGS (including Hot Dry Rock) projects, one of the big challenges was to control (or monitor) the injected water. Diffusion of the injected water caused less recovery rate (Kaieda, 2015) and sometimes linked to induced seismicity (Majer et al., 2007).

For the fluid injection monitoring in EGS fields, a resistivity change due to the hydraulic stimulation by means of Magnetotellurics was detected at Paralana, Australia (Peacock et al., 2012). In contrast, in the case of non-stimulation type of EGS, few resistivity changes near the reservoir was so far monitored by means of Audio Magnetotellurics (Yamaya et al., 2018) during the artificial recharge into the depleted reservoir in Tohoku region, Japan (Okabe et al., 2015). Furthermore, quantitative interpretations for the injected water distribution and water saturation recovery during these injection tests have not been evaluated yet. To monitor the injected water behavior from the geophysical explorations, we should experimentally investigate the basic relationship between the water saturation and physical properties (electric and elastic properties) of rock.

As a first step for more quantitative interpretation of geophysical explorations (e.g., electromagnetic and seismic explorations), we conducted laboratory fluid-flow tests and simultaneous measurements of electric and elastic properties of fractured geothermal reservoir rocks. Electric properties of rocks have been well investigated with porous rock (e.g., Archie, 1942; Knight, 1991; Su et al., 2000; Revil, 2013) and it is empirically known that resistivity ρ is functions of the fluid resistivity ρ_w, porosity φ and water saturation S_w as follows;

$$\rho = a \, \rho_w \, \varphi^{-m} \, S_w^{-n} \tag{1}$$

where a, m and n are coefficients which depend on the characteristics of samples (known as tortuosity factor, cementation factor and saturation exponent, respectively). This equation (Archie's law) has been broadly applied to the interpretation of oil fields and CCS (Carbon Capture and Storage) test fields; however, a problem is that this equation is the empirical law for porous rocks (e.g., sandstone). Furthermore, the effect of frequency on the electric properties of rocks is few investigated (e.g., Rankin and Singh, 1985), and there is no study to investigate frequency dependence during increasing the saturation condition. As for elastic properties of rocks, increases of the velocity and attenuation are experimentally confirmed as water saturation increases (e.g., Murphy, 1982; Endress and Knight, 1991). However, these studies also used porous rocks as the samples. In terms of unsaturated fractured rocks, its electric and elastic properties have not been investigated yet. In addition, most of these previous studies changed the water saturation by evaporative drying. To consider the water recharge into the depleted

reservoirs, the water saturation must be changing from dry (Sw =~0) to wet under a confining pressure. To the best of our knowledge, there is no experimental study to simulate such a EGS condition.

In this study, we firstly developed an experimental system, which simulates EGS (artificial recharge type) conditions and which allowed us to conduct fluid-flow tests by using two types of fractured geothermal rocks. We summarized the experimental system and procedure in the method section, then showed the results of electric (resistivity) and elastic (velocity and amplitude) properties as water saturation increases, and finally discussed effects of the water saturation on the resistivity, velocity and amplitude. We also discussed effects of the porosity, salinity, and frequency on resistivity measurements and implication for the fields.

2. Method

2.1 Sample preparation

Fluid-flow tests were carried out by using a pyroxene andesite, which was sampled from a geothermal field in the southern part of Kyushu island, Japan. From the microscopic observation and X-ray diffraction analysis, it was identified that this sample mainly consists of plagioclase, quartz, calcite and a small amount of clay minerals; 1.3 wt.% of chlorite and 2.6 wt.% of illite-smectite mixed layer minerals were identified by Mineral Intensity Factor analysis (Moore and Reynolds, 1997). From this sample, cylindrical cores (35 mm in diameter and 70 mm long) were taken. In order to investigate the effect of fractures on electric and elastic properties, we prepared two types of specimens;

> Type A: Initially contains vein-like fracture (filled with secondary minerals) and artificially induced thermal cracks
>
> Type B: Initially contains a single natural fracture (open fracture).

Each specimen was cored in parallel with the fractures, which is parallel to the flow direction. Thermal cracks were induced by heating (200 ℃/hour of heating rate, up to 500 ℃ for 1 hour) and cooling (~20 ℃ for 1 hour) the sample (the same method as Yamaguchi and Miyazaki, 1970). The porosity of Type A and Type B specimens are 10.5% and 3.8%, respectively (determined by weighing method). After the specimen were dried for ~24 hours (60 ℃ of oven), four Ag-AgCl electrodes for measuring resistivity and P-wave and S-wave transducers (LiNbO$_3$, 500 kHz) were attached to them. The samples and these attachments were sealed by epoxy resin to separate from confining oil in a pressure vessel.

2.2 Experimental system

Fluid-flow tests and simultaneous measurements of resistivity and elastic wave were conducted by improving the CO$_2$ fluid-flow apparatus at Kyushu university (e.g., Kitamura et al., 2014). The improved experimental system (Figure 1) is mainly composed of a pressure vessel, three syringe pumps for pore-fluid (brine and nitrogen) and confining oil, a media separator for

measuring the water saturation, an Impedance Analyzer SI 1260A (Solartron Analytical, ltd.) for measuring the resistivity, and the elastic wave measurement system (Function Generator, Preamp and A/G Convertor). In the pressure vessel, the sample was connected to the pore-fluid line through a couple of end-pieces and through feedthroughs to the measurement systems of resistivity and elastic wave through feedthroughs.

For the resistivity measurement, we employed the electrical impedance method by four electrodes. Electrical impedance $Z(f)$ is expressed as a following equation by using imaginary unit i.

$$Z(f) = Z(f)' + iZ(f)'' \tag{2}$$

In this study, real and imaginary parts of electrical impedance, $Z(f)'$ and $Z(f)''$, were measured by the Impedance Analyzer for various frequency f. Phase angle θ and resistivity $\rho(f)$, we call it "complex resistivity" hereafter, are calculated as follows;

$$\theta = \tan^{-1}\frac{Z(f)''}{Z(f)'} \tag{3}$$

$$\rho(f) = Z(f)\frac{\pi D^2}{4L} = \rho(f)' + i\rho(f)'' \tag{4}$$

where D and L denote a diameter of a specimen and the distance between the potential electrodes, respectively. In this experiment, applied voltage was set to AC 30 mV and measurement frequency was ranging between 10^{-2} and 10^5 Hz.

Elastic wave was measured by pulse transmission method (input trigger is 250 kHz of frequency and 10Vp-p of amplitude). Obtained waveforms were stacked 200 times and analyzed to calculate the velocity and amplitude, respectively. Elastic wave velocity was calculated from the first arrival traveltime, trigger time and the distance between transmitter and receiver transducers. Amplitude changes of elastic wave were estimated by power spectrum analysis using FFT (Fast Fourier Transform). In this study, the power spectrum was analyzed in 1 period of the first arrival waveforms. The peak of the power spectrum was normalized by the peak value before brine injection (dry condition). Hereafter we call this normalized peak of the power spectrum as "relative amplitude change".

2.3 Experimental procedure

We conducted following three fluid-flow tests in our experiments;

(i) High-salinity brine imbibition (1 wt.%-KCl, 1.75 S/m of electrical conductivity) of Type A specimen (data from Sawayama et al., 2018)

(ii) High-salinity brine imbibition (1 wt.%-KCl, 1.75 S/m of electrical conductivity) of Type B specimen

(iii) Low-salinity brine imbibition (0.1 wt.%-KCl, 0.19 S/m of electrical conductivity) of Type B specimen

Before conducting each fluid-flow test, nitrogen gas (pore pressure; P_p = 1 MPa) was injected into the sample at a confining pressure (P_c) of 11 MPa. This nitrogen gas emulates the superheated steam in a depleted reservoir. Subsequent to the gas saturation, Pc and Pp were

increased to 20 MPa and 10 MPa, respectively. After keeping these conditions constant for few hours, brine was injected into the sample at an injection pressure P_{in} = 11 MPa. After flow rate of drainage fluid became stable, P_{in} was changed step by step to P_{in} = 12, 14, and 16 MPa. The simulated EGS condition in this study means this water injection into the dry gas within fractures under a confining pressure.
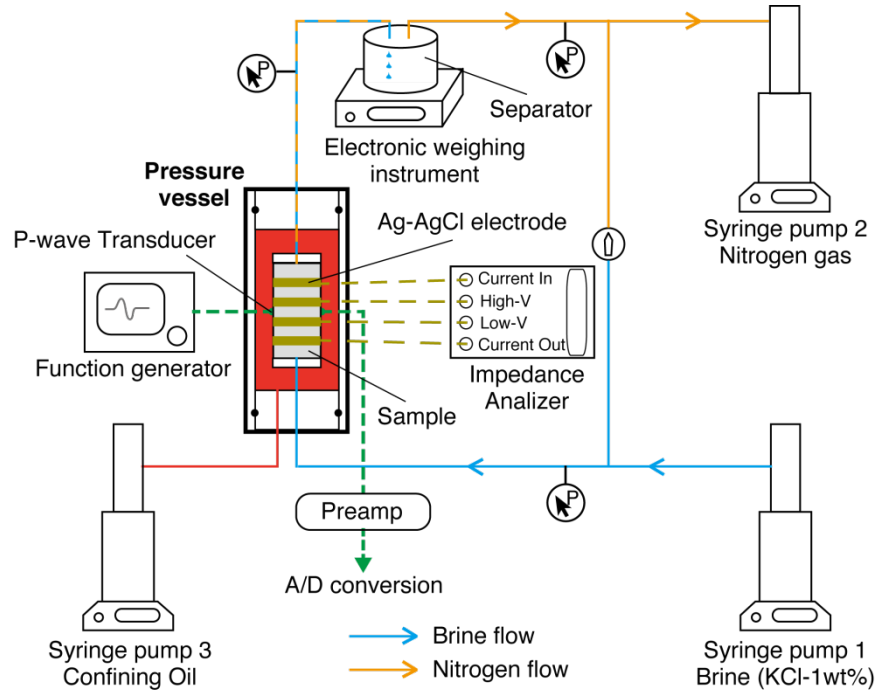

Figure 1: System outline of fluid-flow tests

Since the drainage fluid was a two-phase mixture of brine and nitrogen in our experiments, it was separated by the separator and each volume of brine (V_b^{out}) and nitrogen (V_n^{out}) was measured by means of an electronic weighing instrument and a syringe pump, respectively. From these volumes as well as from the injected brine volume (V_b^{in}), we can estimate the brine volume in a sample (V_b^{sam}) as follows.

$$V_b^{sam} = V_b^{in} - V_b^{out} = V_n^{out} \qquad (5)$$

From the ratio of V_b^{sam} and pore volume, we can calculate the water saturation S_w. The uncertainty of this estimation is approximately ±1% based on fluid volume fluctuations in our experiments. And by monitoring volume changes in each fluid, we also obtained flow rates and thereby calculated permeability (k) from darcy's law;

$$\frac{Q}{A} = \frac{k}{\mu}\frac{dp}{dx} \qquad (6)$$

where Q, A, μ and dp/dx are flow rate (in this study, brine output flow rate), cross sectional area, viscosity and pressure gradient, respectively. Note that k here represents "effective" permeability because fluid-flow tests in this study were conducted under two-phase flow.

3. Results and Discussion

3.1 Fluid-flow test

Figure 2 shows the result of pressure and volume changes against the elapsed time during the fluid-flow test of Type A specimen. The slopes of each fluid volume change, which indicates that flow rates increased with injection pressure. The volume change of brine output became increasing after ~15000 s, indicating that pre-filled nitrogen in a main path was almost released and injected brine started to flow downward at this point. From the flow rate of brine output, (effective) permeability k was calculated and plotted against the injection pressure (Figure 3). Permeability of both Type A and B specimen shows almost no (injection) pressure dependence. This suggests that the main fluid pathway, which is thought to be a macroscopic fracture within a specimen, was not influenced by pressure. Comparing the permeability results of both specimens, permeability of Type B specimen was ~1 order higher than that of Type A specimen. And hence, water saturation change of Type B specimen was also much faster than that of Type A specimen.
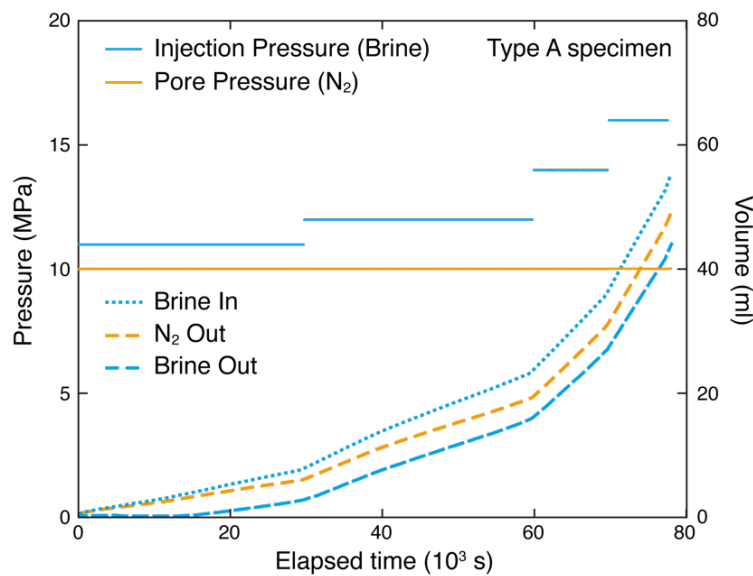

Figure 2: Temporal changes of the fluid pressures and volumes of Type A specimen (data from Sawayama et al., 2018). Solid lines indicate the brine injection pressure (light blue) and nitrogen pressure (orange). The light blue dotted line depicts the volume of the brine that was injected, whereas the dashed lines depict the drainage volumes of nitrogen (orange) and brine (light blue). Note that the drainage fluid was separated into nitrogen and brine using a separator (Figure 1).
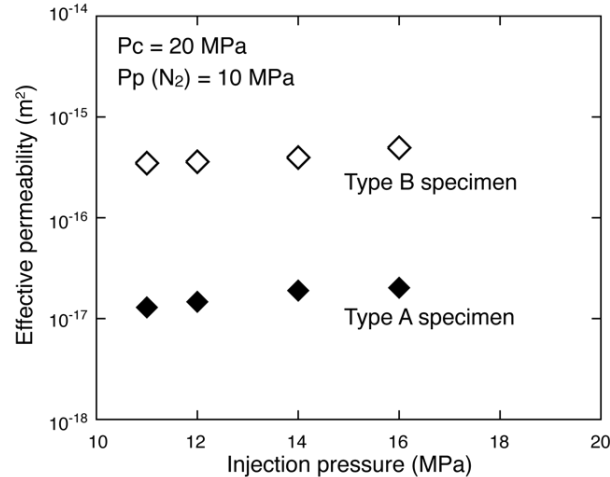
Figure 3: Effective permeability changes as a function of brine injection pressure. Black and white marks represent the results of Type A (data from Sawayama et al., 2018) and B specimen, respectively.

3.2 Electric property

Figure 4 shows the bode plot of the complex resistivity under various conditions of Type A specimen (1 wt.%-KCl brine). The complex resistivity dramatically decreased after brine injection (Figure 4 a) and slightly decreased with increasing brine injection pressure (Figure 4 b). The change of the complex resistivity during the gas-brine replacement, which was investigated in this study, was much more pronounced than that of brine-oil replacement within sandstone (Liu et al., 2015). This suggests that the water penetration into the depleted dry rocks could be detected as a remarkable change of the resistivity.

3.2.1 Effect of water saturation on the resistivity

The effect of injection pressure on the complex resistivity (Figure 4 b) is thought to reflect the effect of saturation on it. Thus, we plotted the complex resistivity as a function of the estimated water saturation, which continuously changed with increasing injection pressure (Figure 5). As a result, the complex resistivity at each pressure level showed continuous decreases with increasing water saturation. While the most typical case is Figure 5 a (resistivity of Type A specimen at 10 mHz of frequency, 1 wt.% of salinity), a similar trend was seen in the Type B specimen at the same salinity condition (Figure 5 b). Comparing the results from Type A specimen with Type B specimen for the same salinity and water saturation, the resistivity of Type A specimen (Figure 5 a) is 1 order lower than that of Type B specimen (Figure 5 b). This gap might be caused by porosity difference of Type A specimen (10.5%) and Type B specimen (3.8%). In the complex resistivity of Type B specimen at the lower salinity condition (Figure 5 c, 0.1 wt.%-KCl brine), we also detected a logarithm relationship at a water saturation higher than 25%, while it was scattered at lower saturation. Since the Type B specimen is relatively less porous, the total number of ions, which are thought to be a conductor of electricity, is reduced at lower saturation and lower salinity condition and the quality of resistivity measurements at such a condition might become insufficient. The resistivity of the higher salinity condition (Figure 5 b) was almost a half of that of the lower salinity (Figure 5 c) at same water saturation (higher than 25% water saturation). This reflects that the resistivity depends not only on water saturation,

but is also highly influenced by the porosity and salinity, which is consistent with previous studies (e.g., Sen et al., 1988; Revil and Glover, 1998).
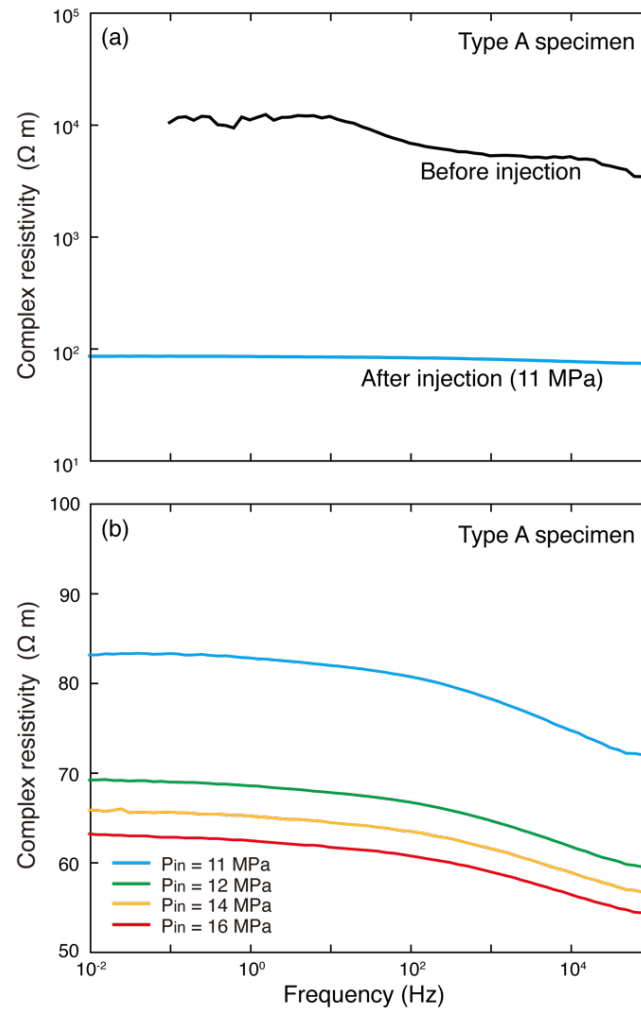

Figure 4: Complex resistivity against the frequency (bode plot) under various injection pressure of Type A specimen (data from Sawayama et al., 2018). (a) Complex resistivity changes of before and after brine injection at 11 MPa and (b) complex resistivity at various injection pressures, P_{in}.
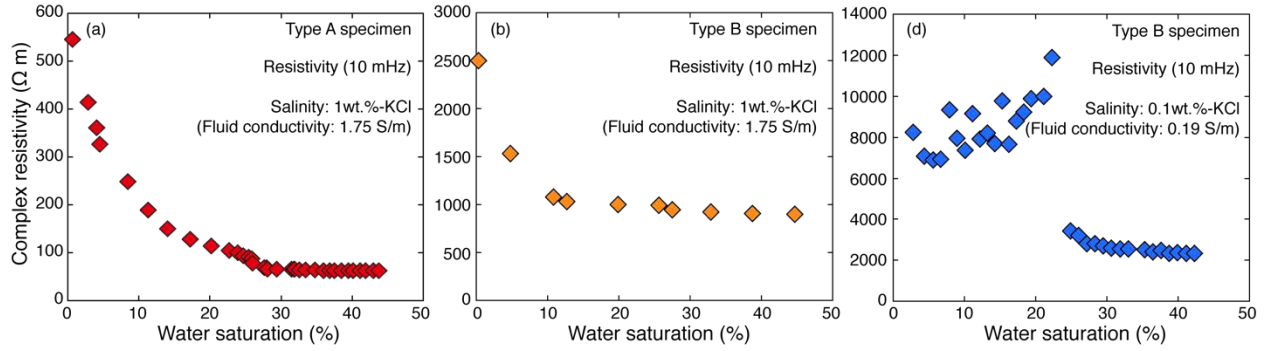
Figure 5: Decrement of the complex resistivity with increasing water saturation. (a) Type A specimen (data from Sawayama et al., 2018), (b) Type B specimen at higher salinity (1 wt.%-KCl brine) condition and (c) Type B specimen at lower salinity (0.1 wt.%-KCl brine) condition. The data of resistivity was calculated from the electrical impedance at 10 mHz of frequency.

In order to characterize the trends of all resistivity results in detail, we applied Archie's relation on our experimental results. Here, we calculated Resistivity Index (RI) for each condition as following equation;

$$\text{RI} = \frac{\rho}{\rho_{\text{sat}}} = S_w^{-n} \tag{7}$$

where ρ_{sat} is the resistivity at fully saturated ($S_w = 1$). Figure 6 shows Resistivity Index (RI) against the water saturation under various experimental conditions. In each condition, log-log relationships between RI and saturation were almost linear, as follows;

$$\text{RI}_{\text{B,low}} = S_w^{-1.15}, \quad (\text{R}^2 = 0.82) \tag{8}$$

$$\text{RI}_{\text{B,high}} = S_w^{-0.28}, \quad (\text{R}^2 = 0.66) \tag{9}$$

$$\text{RI}_{\text{A,high}} = S_w^{-0.35}, \quad (\text{R}^2 = 0.78) \tag{10}$$

here, $\text{RI}_{\text{B,low}}$, $\text{RI}_{\text{B,high}}$ and $\text{RI}_{\text{A,high}}$ denote each condition of Type B specimen at 0.1 wt.%-KCl brine (low salinity), Type B specimen at 1 wt.%-KCl brine (high salinity), and Type A specimen at 1 wt.%-KCl brine (high salinity), respectively. The coefficient of determination for each condition, R^2, was relatively high, indicating that our experimental results are in somehow good agreement with Archie's relation. Our results show that the saturation exponent n gives much smaller values than the result, which was previously reported (for sandstone under brine-oil replacement, $n = $ ~2; Guéguen and Palciauskas, 1994). Although some studies reported that the saturation exponent n can be varied by pore characteristics (e.g., for sandstone, $n = $ ~1−4; Liu et al., 2015) and pore fluid medium (e.g., for oil, $n = $ ~1−3; Schmutz et al., 2012), these values are higher than our results ($n < $ ~1). Our experimental results indicate that RI under gas-brine replacement could have more moderate slope than that under brine-oil replacement. As indicated in these previous studies, our results also showed different values of n under different porosity (eq. 9 and 10) as well as salinity (eq. 8 and 9). Furthermore, even the salinity and porosity are the same condition (red marks), it is difficult to fit as a slope; it looks like rather than two linear relations. This change of Archie's relation might reflect that fluid-flow pathways changed at the point (see *3.3* for detail).
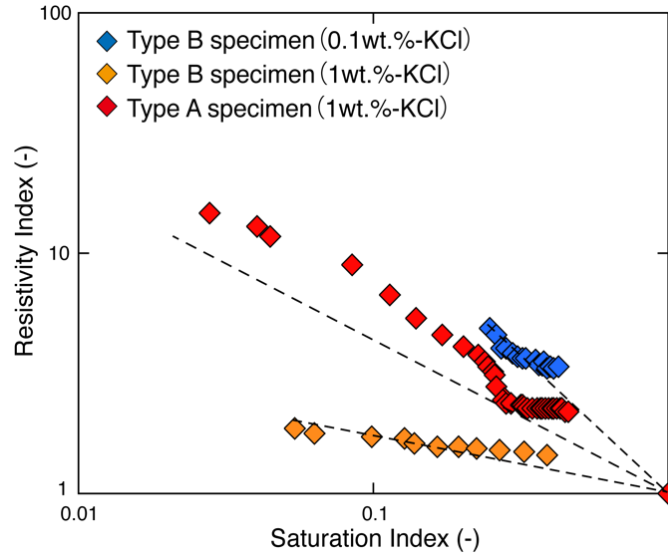
Figure 6: Log-log relationship between Resistivity Index and Saturation Index under various experimental conditions. Saturation Index here denotes the water saturation of which maximum value is 1 (not expressed as a percentage). Dashed lines depict the logarithmical approximation lines in Archie's relation.

3.2.2 Effects of total number of ions on the resistivity

In Archie's relation, it is difficult to express the effects of salinity, porosity and water saturation on the resistivity in one and the same diagram (Figure 6). Thus, to depict these effects on the resistivity, we calculated the total number of ions within a specimen which contains all the information about salinity, porosity and water saturation. In this study, the brine we used was only KCl solution, which contained ionized K^+ and Cl^-. If KCl was totally ionized and there were no other ion species within a specimen, total number of ions within a specimen (N_{ion}) is equal to the double of moles of KCl (N_{KCl}). Therefore, the total number of ions can be calculated as following

$$N_{ion} = 2\, N_{KCl} = 2\, \varphi V S_w C \qquad\qquad (11)$$

with φV is the pore volume and C represents the molarity, which is calculated from the salinity. Figure 7 shows the complex resistivity change as a function of the calculated total number of ions. Although it is slightly fluctuating, the log-log relationships of all three datasets is almost linear;

$$\rho = 23.8\, N_{ion}^{-0.43} = 47.6\, \varphi V S_w C^{-0.43}, \quad (R^2 = 0.97) \qquad\qquad (12)$$

with much higher coefficient of determination R^2 than Archie's relation (eq. 8−10). In Archie's law (eq. 1), it is obvious that the resistivity is influenced many factors such as porosity, water saturation, fluid resistivity (or salinity) and three coefficients (*a*, *m* and *n*), which depend on specific structural and textural sample characteristics derived empirically. Our simple model indicates that relating the complex resistivity to the number of free charge carriers within the sample, may describe the dependence of resistivity on porosity, salinity, and saturation more easily. Hence, this may lead to a more quantitative interpretation of exploration data (e.g.,

Magnetotellurics) in the field. Although further studies are needed to confirm this relationship, there is no systematic study to investigate the effects of salinity, porosity and water saturation on the resistivity simultaneously. As the other effects on the resistivity, it is affected by the temperature (Sen and Goode, 1992) and rock type or mineral assembly (Shen et al., 1986), and hence, at least, a y-intercept (in this study, 47.6 Ω m) must be changed due to such a condition.
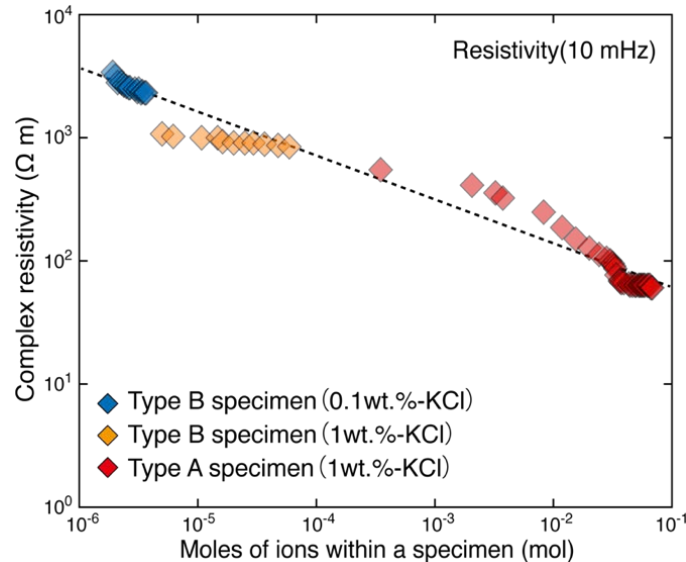

Figure 7: Log-log relationship between the complex resistivity and total number of ions calculated by various experimental conditions. Dotted line depicts a logarithmical approximation line.

3.2.3 Effect of frequency on resistivity measurement

We also investigated the frequency dependence of the resistivity-saturation relationship. Figure 8 shows the typical complex resistivity changes against the water saturation (Type A specimen) and each value was normalized by the initial. Almost no changes of the complex resistivity were observed in the various ranges of frequency. This result is not consistent with a previous study which reported that the relationship between the water saturation and the electric conductivity has a frequency dependence (Ullrich and Slater, 2004). In terms of frequency dependence on the real part of the dielectric constant, it was reported to show a stronger frequency dependence as the clay contents increase (Rankin and Singh, 1985). Our sample contains less clay minerals (3.9 wt.%), and hence remarkable frequency dependence could not be seen in our experimental results. This suggests that the frequency dependence of the resistivity during the water penetration into the clay-free rock layer might be negligible.
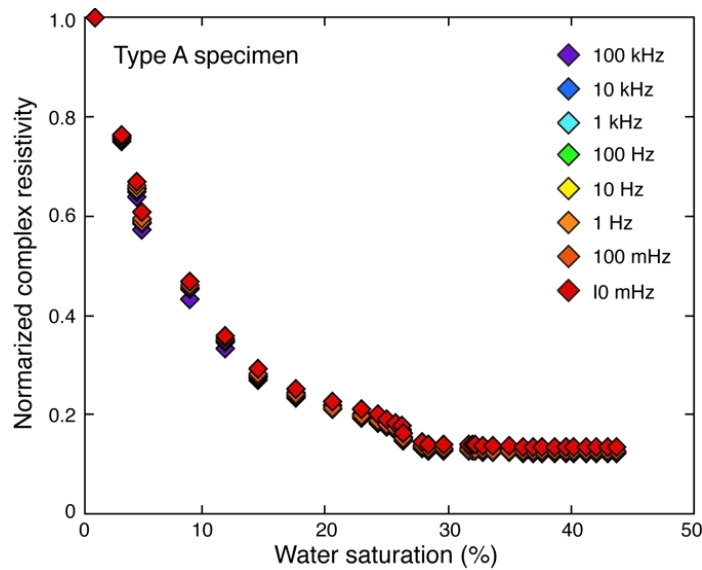
Figure 8: Frequency dependence of the relationship between complex resistivity and water saturation of Type A specimen (data from Sawayama et al., 2018) in the frequency range of $10^{-2}–10^5$ Hz. The values of the complex resistivity in each frequency are normalized by maximum (initial) value in each frequency.

3.3 Elastic property

Figure 9 shows all waveforms recorded during the measurement of Type A and B specimen. As water saturation increases (plot color changes red to blue), Type A specimen (a) shows the variation whereas Type B specimen (b) does not show any changes. Furthermore, first arrival traveltime of Type B specimen (~7 μs) is much higher than that of Type B specimen (~10 μs), indicating that elastic wave of Type B specimen might not detect the thin fracture. As we mentioned in *2.1*, Type A specimen contains the fracture and multi thermal cracks whereas Type B specimen contains only a thin fracture (in the direction of wave measuring path). This may result in the saturation dependence of Type A specimen and saturation independence of Type B specimen. In type A specimen, subsequent waves showed an obvious increase of the attenuation and delay of the traveltime, might reflecting the S-wave element (Mavko et al., 2009). However, since subsequent waves contain many unknown effects such as reflections and surface waves (Yoshimitsu et al., 2016), we did not discuss the subsequent waves, but only focus on first arrival P-waves. Therefore, we dealt with only the first arrival data of Type A specimen (~10−12 μs of time) for following discussions of the velocity and amplitude changes.
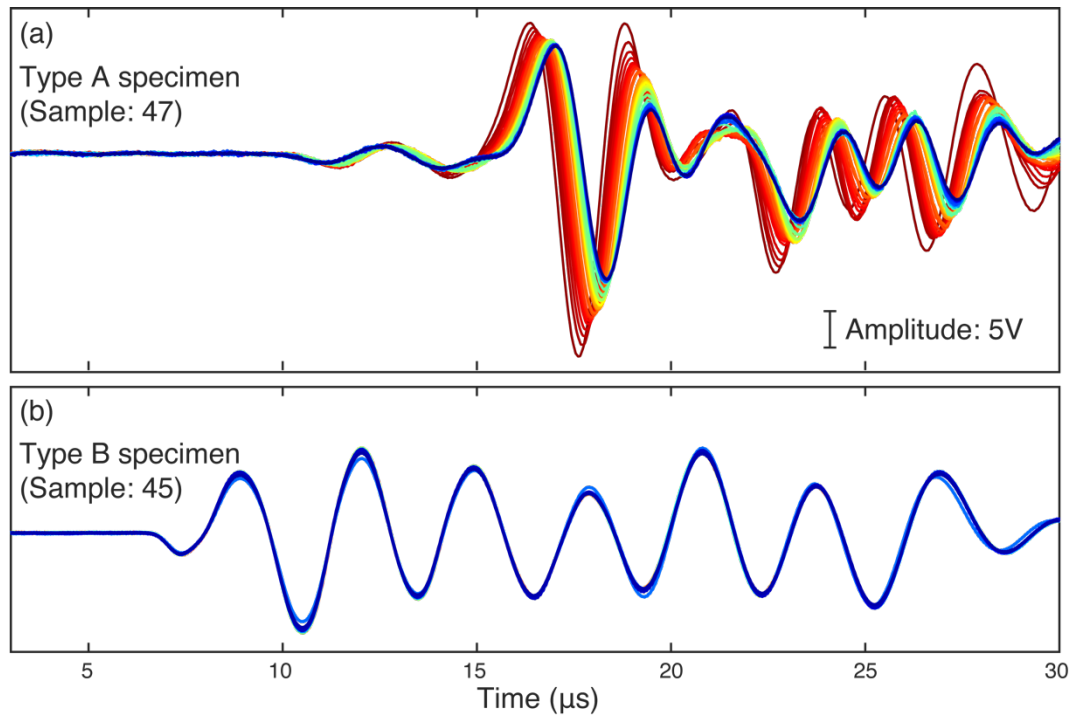
Figure 9: All waveforms of (a) Type A and (b) Type B specimen during increasing the water saturation. Note that plot colors change from red to blue as water saturation increases.

Elastic wave velocity (P-wave velocity) of Type A specimen was calculated by first arrival traveltime (~10 μs of time) and plotted against the water saturation (Figure 10). The velocity did not show significant change when the water saturation increased, whereas a slight velocity increase was detected between 25−28% of water saturation. This small increase occurred when injection pressure increases. Therefore, this might reflect the penetration of brine into the tiny thermal cracks, branching off the main flow path and which are thought to be saturated by increasing the injection pressure. This change is consistent with the timing when the slope of Resistivity Index changed (Figure 6). While the velocity detects this penetration to the cracks, it has less sensitivity for the water saturation compared with the resistivity (Figure 5). In the brine-CO_2 drainage tests of sandstones, lower sensitivity of the P-wave velocity was reported at the lower saturation (S_w <~20%) whereas the resistivity shows continuous changes at any saturation conditions (Nakatsuka et al., 2010). This sensitivity of P-wave velocity must be caused by the variation of Bulk modules against the water saturation (Gassmann's relations; Mavko et al., 2009).

Although velocity changes against the water saturation were not clearly detected, the relative amplitude changes significantly. Power spectrum analysis showed a continuous decrease against the water saturation (Figure 11). This might be related to the attenuation increase with water saturation, which was confirmed in a previous study with porous rocks (e.g., Murphy, 1982; Zhang et al., 2016). Therefore, amplitude (or attenuation) could have a potential to detect small changes in the water saturation which cannot be detected by the velocity.
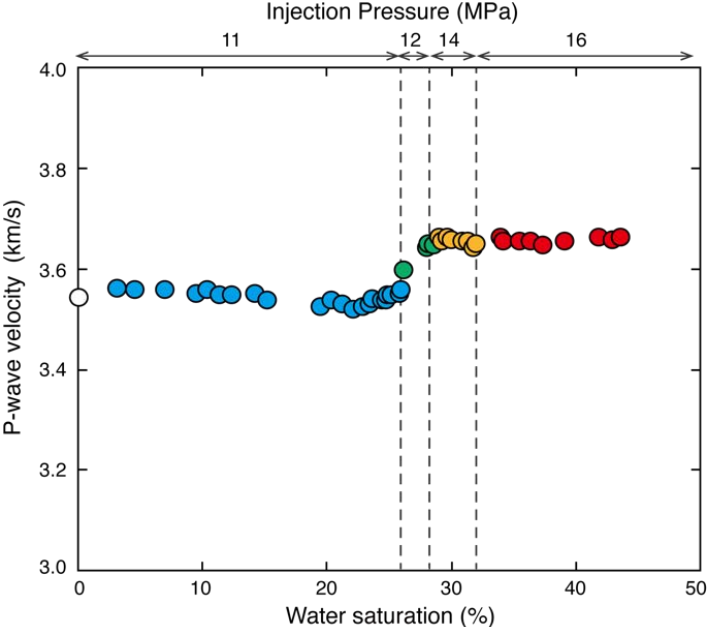
Figure 10: Changes of P-wave velocity plotted against the water saturation.
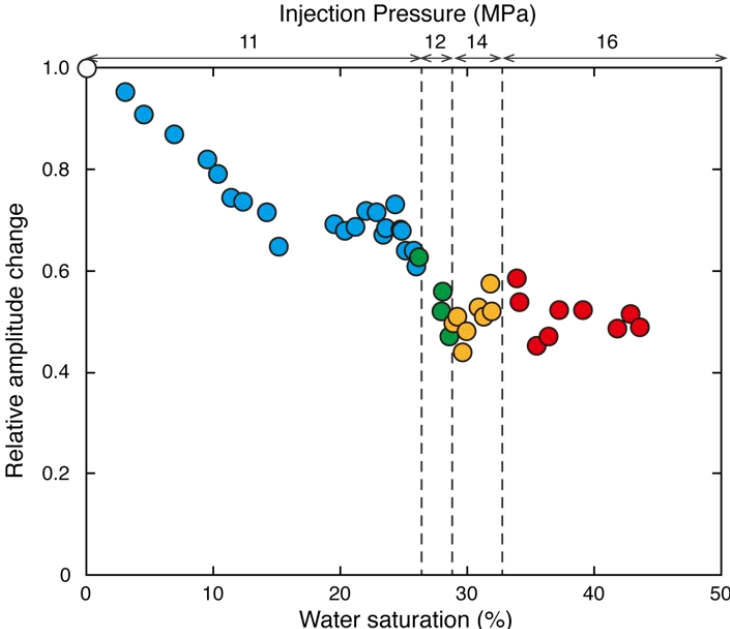

Figure 11: Relative amplitude changes which is the peak of normalized power as a function of the water saturation.

4. Conclusion

We developed an experimental system, which simulates EGS condition (gas to brine replacement) and allows to simultaneously measuring the changes of electric and elastic properties with increasing the water saturation. As a result, the complex resistivity dramatically decreased after the brine injection and showed almost no frequency dependence on it. This suggests that water penetration into the depleted dry rocks could be detected as a remarkable change of the resistivity in the EGS fields. Whereas the resistivity showed clear logarithmic relationship with the water saturation, effects of the salinity and porosity on the resistivity were also observed. These effects of water saturation, salinity and porosity could be explained by the total number of ions within a specimen, and we proposed this new relationship to reduce unknown parameters for the better interpretation of geophysical explorations in the fields. Elastic wave velocity showed almost no saturation dependence, while it has a sensitivity for the infiltration of the new fluid path. In contrast, relative amplitude change decreased as water saturation increases, and hence amplitude (or attenuation) could have potential to detect small changes of the water saturation which cannot be detected by the velocity.

To apply our results to the actual EGS field, we must considerer the temperature effects. In the previous study of oil-bearing sands, the temperature effect on the velocity and electric conductivity were almost linear (Martinez et al., 2012). However, their temperature ranges were small (20−70 ℃). Wide ranges of temperature effects, including higher temperature of EGS conditions(~250 ℃), should be investigated in the next step of our studies.

REFERENCES

Archie, E, G. "The Electrical Resistivity Log as an Aid in Determining Some Reservoir Characteristics." Petroleum Technology, (1942), 54–62.

Endres, A. L. and Knight, R. "The effects of pore-scale fluid distribution on the physical properties of partially saturated tight sandstones." Journal of Applied Physics, 69(2), (1991), 1091−1098.

Guéguen, Y. and Palciauskas, V. "Introduction to the physics of rocks." Princeton, New Jersey, (1994), 294p.

Kaieda, H. "Multiple Reservoir Creation and Evaluation in the Ogachi and Hijiori HDR Projects, Japan." Proceedings of the World Geothermal Congress 2015, (2015).

Kitamura, K., Jiang, F., Valocchi, A. J., Chiyonobu, S., Tsuji, T. and Christensen, K. T. "The study of heterogeneous two-phase flow around small-scale heterogeneity in porous sandstone by measured elastic wave velocities and lattice Boltzmann method simulation." Journal of Geophysical Research: Solid Earth, 119, (2014), 7564−7577.

Knight, R. "Hysteresis in the electrical resistivity of partially saturated sandstones." Geophysics, 56(12), (1991), 2139–2147.

Liu, Y., Xue, Z., Park, H., Kiyama, T., Zhang, Y., Nishizawa, O. and Chae, K. seok. "Measurement of electrical impedance of a Berea sandstone core during the displacement of saturated brine by oil and CO2 injections." Journal of Applied Physics, 123, (2015), 50–62.

Majer, E. L., Baria, R., Stark, M., Oates, S., Bommer, J., Smith, B. and Asanuma, H. "Induced seismicity associated with Enhanced Geothermal Systems." Geothermics, 36, (2007), 185–222.

Martinez, Fernando J., Michael L. Batzle, and André Revil. "Influence of temperature on seismic velocities and complex conductivity of heavy oil-bearing sands." Geophysics, 77(3), (2012), 19−34.

Mavko, G., Mukerji, T. and Dvorkin, J. "The Rock Physics Handbook Tools for Seismic Analysis of Porous Media." Cambridge University Press, Cambridge, (2009), 511p.

Moore, D. M. and Reynolds, R. C. "X-ray Diffraction and the Identification and Analysis of Clay Minerals." Oxford University Press, New York, (1997), 378p.

Murphy, W. F. "Effects of partial water saturation on attenuation in Massilon sandstone and Vycor porous glass." Journal of the Acoustical Society of America, 71(6), (1982), 1458-1468.

Nakatsuka, Y., Xue, Z., Garcia, H., and Matsuoka, T. "Experimental study on CO2 monitoring and quantification of stored CO2 in saline formations using resistivity measurements." International Journal of Greenhouse Gas Control, 4(2), (2010), 209–216.

Okabe, T., Sato, T., Osato, K., Saeki, K., Sakaguchi, K. and Fujimoto, K. "Current Status of Technology Development for Geothermal Reservoir Evaluation and Management." World Geothermal Congress 2015, (2015).

Peacock, J. R., Thiel, S., Reid, P. and Heinson, G. "Magnetotelluric monitoring of a fluid injection: Example from an enhanced geothermal system." Geophysical Research Letters, 39(17), (2012), 3–7.

Rankin, D. and Singh, R. P. "Effect of clay and salinity on the dielectric properties of rock." Journal of Geophysical Research, 90(B10), (1985), 8793–8800.

Revil, A. "Effective conductivity and permittivity of unsaturated porous materials in the frequency range 1 mHz-1GHz." Water Resources Research, 49(1), (2013), 306–327.

Revil, A. and Glover, P. W. J. "Nature of surface electrical conductivity in natural sands, sandstones, and clays." Geophysical Research Letters, 25(5), (1998), 691–694.

Sawayama, K., Kitamura, K. and Fujimitsu, Y., "Relationship between Complex Resistivity, Elastic Wave and Water Saturation of Cracked Andesite under Laboratory Fluid-Flow Test." Exploration Geophysics, (2018), in Japanese with English abstract, in press.

Sen, P. N. and Goode, P. A. "Influence of temperature on electrical conductivity on shaly sands" Geophysics, 57(1), (1992), 89–96.

Sen, P. N., Goode, P. A. and Sibbit, A. "Electrical conduction in clay bearing sandstones at low and high salinities." Journal of Applied Physics, 63(10), (1988), 4832–4840.

Shen, L. C., Savre, W. C., Price, J. M. and Athavale, K. "Dielectric properties of reservoir rocks at ultra-high frequencies." Geophysics, 50(4), (1986), 692–704.

Schmutz, M., A. Blondel, and A. Revil. "Saturation dependence of the quadrature conductivity of oil-bearing sands." Geophysical Research Letters, 39(3), (2012), 1–6.

Su, Q., Feng, Q. and Shang, Z. "Electrical impedance variation with water saturation in rock." Geophysics, 65(1), (2000), 68–75.

Ullrich, C. and Slater, L. D. "Induced polarization measurements on unsaturated, unconsolidated sands." Geophysics, 69(3), (2004), 762–771.

Yamaguchi, U. and Miyazaki, M. "A study of the strength or failure of rocks heated to high temperature." Journal of MMIJ, 86, (1970), 346–351, in Japanese with English abstract.

Yamaya, Y., Takakura, S., Asanuma, H. "Resistivity monitoring of a geothermal reservoir at the Okuaizu geothermal field, Japan using the AMT method." Journal of the Geothermal Research Society of Japan, (2018), in Japanese with English abstract (in press).

Yoshimitsu, N., Furumura, T. and Maeda, T. "Geometric effect on a laboratory-scale wave field inferred from a three-dimensional numerical simulation." Journal of Applied Physics, 132, (2016), 184–192.

Zhang, Y., Park, H., Nishizawa, O., Kiyama, T., Liu, Y., Chae, K. and Xue, Z. "Effects of fluid displacement pattern on complex electrical impedance in Berea sandstone over frequency range 104-106 Hz." Geophysical Prospecting, 65, (2016), 1053–1070.